physica status solidi pss b
www.pss-b.com

Check for updates

n-Doped InGaP Nanowire Shells in GaAs/InGaP Core–Shell p–n Junctions

Lisa Liborius, Jan Bieniek, Andreas Nägelein, Franz-Josef Tegude, Werner Prost, Thomas Hannappel, Artur Poloczek, and Nils Weimann*

Herein, the characterization of n-doped InGaP:Si shells in coaxial not-intentionally doped (nid)-GaAs/n-InGaP as well as n–p–n core–multishell nanowires grown by metalorganic vapor-phase epitaxy is reported. The multi-tip scanning tunneling microscopy technique is used for contact-independent resistance profiling along the tapered nid-GaAs/n-InGaP core–shell nanowires to estimate the established emitter shell doping concentration to $N_D \approx 3 \cdot 10^{18}\,cm^{-3}$. Contacts on these shells are demonstrated and exhibit ohmic current–voltage characteristics after annealing. Application potential is demonstrated by the growth and processing of coaxial p-GaAs/n-InGaP junctions in n–p–n core–multishell nanowires, with n-InGaP being the electron-supplying emitter material. Current–voltage characteristics and temperature-dependent electroluminescence measurements substantiate successful doping of the n-InGaP shell. A tunneling-assisted contribution to the leakage currents of the investigated p–n junctions is verified by the sub-bandgap luminescence at low temperatures and is attributed to radiative tunneling processes.

1. Introduction

The application of p–n junction-based semiconducting nanowires (NW) in electronic and optoelectronic devices is promising due to their unique geometry. Axial or coaxial p–n junctions in III–V NW structures are available for a number of material systems such as InP, GaN, and GaAs.[1–3] Solar cells and light-emitting diodes (LED) are prominent examples for well-researched structures with homo- or heterojunctions as active regions.[4–9] The small footprint of the NWs and the resulting ability to compensate strain by lateral expansion enables the combination with different technology platforms, e.g. monolithic integration on Si.[9,10] Implementation of heterojunctions enables bandgap engineering in NW structures by the adjustment of band discontinuities to a specific device application.[5,11,12] For GaAs-based heterostructures in particular, AlGaAs and GaAsP offer discontinuities in both valence and conduction band, whereas in InGaP the discontinuity almost solely manifests in the valence band making it a suitable candidate for a wide band gap electron emitter.[11–13] GaAs/InGaP NW LEDs on Si and GaP substrates have been demonstrated, with InGaP:Si cladding as the n-type region and not-intentionally doped (nid) GaAs core as the active region.[5] The InGaP shell can also be beneficial regarding surface recombination of charge carriers due to a possible wide band gap passivation. This effect is reported for various NW devices, e.g. regarding the efficiency enhancement of GaAsP solar cells or GaAs photodetectors.[4,14] Despite all the progress made, the full potential of III/V NW axial and radial heterostructures has not been explored and limitations in NW growth, doping, and heterostructure complexity are currently under investigation.[15–17]

For example, until today NW devices containing one p–n junction only have been reported, mostly.[1–8] An extension of a single p–n structure by an additional junction allows the realization of a bipolar transistor. The principle function of a NW heterojunction bipolar transistor (NW-HBT) was previously demonstrated by our group.[18] Herein, InGaP is included in a n–p–n core–multishell NW structure serving as a passivation and an electron-supply material with a hole-blocking character at the heterojunction.[13] The device performance of bipolar transistors is strongly dependent on the layer thickness and doping concentration, thus the determination of material and technological parameters are essential. No experimental data regarding doping concentration in n-InGaP shells have been published, so far.

The standard determination of doping concentration by Hall measurement is challenging in NW structures because of the small diameter and the according difficulty regarding contact definition.[19–21] Analyses of charge carrier mobilities by Hall measurements have been reported for various NW structures

L. Liborius, J. Bieniek, Prof. F.-J. Tegude, Dr. W. Prost, Dr. A. Poloczek, Prof. N. Weimann
Components for High Frequency Electronics (BHE)
University of Duisburg-Essen
Lotharstr. 55, 47057 Duisburg, Germany
E-mail: lisa.liborius@uni-due.de

A. Nägelein, Prof. T. Hannappel
Fundamentals of Energy Materials
Technische Universität Ilmenau
Gustav-Kirchhoffstr. 5, 98693 Ilmenau, Germany

The ORCID identification number(s) for the author(s) of this article can be found under https://doi.org/10.1002/pssb.201900358.

DOI: 10.1002/pssb.201900358

consisting of one material core as well as for core–shell NWs, including the materials GaAs/InAs and InP.[19–24] Alternative approaches, such as the commonly used transmission line method or field effect mobility measurements, require the formation of uniform semiconductor regions between ohmic contacts or a homogeneous charge distribution inside the semiconductor, which is difficult to achieve on core–shell NWs that exhibit a tapered diameter.[25–31] One major disadvantage of the techniques mentioned earlier is the requirement of good contacts with the semiconductor, as an ohmic contact formation can prove difficult and may alter the composition and doping at the metal semiconductor interface, influencing the measured results.[32,33] Therefore, measurement techniques independent of contact formation are favorable.

Optical methods such as photoluminescence, Raman or optical pump terahertz-probe spectroscopy are utilized as alternatives, as they require no processing of contacts.[34–38] However, depending on the crystal structure and the semiconducting materials used, the data interpretation can be challenging as there might not be bulk references. And, in core–shell NWs, depending on the excitation energy, the shell and core materials are penetrated simultaneously, which further complicates the analysis. Electrical analysis by scanning probe microscopy allows for contact-independent doping profiling of semiconductors via scanning capacitance measurements and has been used for electrical NW characterization.[39,40] Another technique is the ultrahigh vacuum (UHV) multi-tip scanning tunneling microscopy (MT-STM), which offers the possibility to enable contact area-independent resistance profiling along tapered NWs when used as a four-point prober.[27,41,42] The doping concentration can then be derived from a simple resistance model, without the necessity to consider contact resistances.

Implementation of n-doped InGaP NW shells in coaxial p–n devices requires high-quality ohmic contacts. Although ohmic contacts with n-GaAs NWs have been demonstrated, there are only few publications mentioning Ge/Au contacts with n-InGaP NW shells, and the quality of the contacts has not been analyzed.[4,5] Ohmic Ge/Au-based contacts with planar n-InGaP have been used for many years.[43,44] However, to obtain a linear *I*–*V* response with low contact resistances, usually a high annealing temperature is necessary, which allows for diffusion of Ge into the semiconductor to narrow the potential barrier at the metal–semiconductor interface. This is critical for contacts with NWs with Ga-content due to the increased exchange of Ge and Ga atoms at temperatures above 320 °C, which could affect the NW morphology near the metal/NW interface.[45]

Herein, we report on the analysis of Si-doped InGaP NW shells grown by metalorganic vapor-phase epitaxy (MOVPE) regarding charge carrier concentration, ohmic contacts to these shells, and their doping-dependent influence on the current transport through GaAs/InGaP heterojunctions.

2. Results and Discussion

Two different NW heterostructures are grown, processed, and analyzed in this study (details in Experimental Section 4). Their schematic structure and cross section scanning electron microscope (SEM) and scanning transmission electron microscopy (STEM) images are depicted in **Figure 1**a,b.

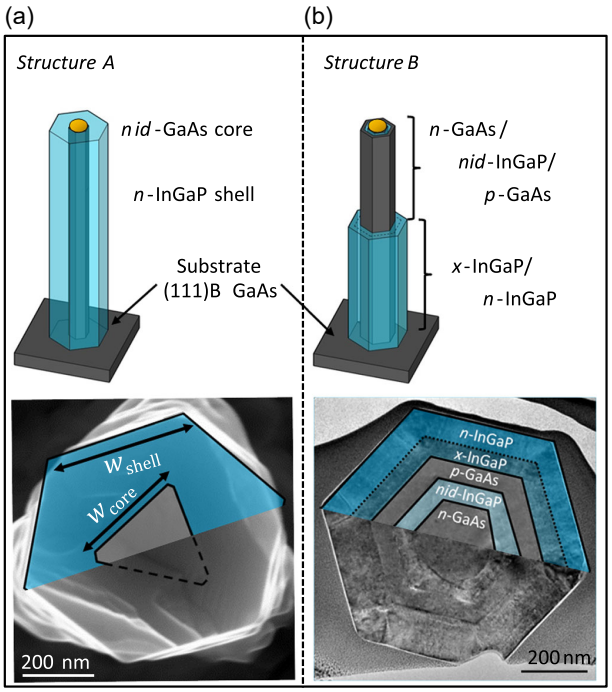

Figure 1. Schematic structure and cross section images (illustrated in false colors) of the analyzed NW samples. a) *Structure A* with nid-GaAs core and n-InGaP shell for material analysis. The SEM image shows the cross section with non-symmetric hexagonal core (estimated as triangle) and symmetric hexagonal shell geometry. b) *Structure B* as n-GaAs/nid-InGaP/p-GaAs/x-InGaP/n-InGaP core–multishell NW for device application. The hexagonal cross section is analyzed by STEM imaging.

2.1. Estimation of Donor Concentration

For the estimation of the doping concentration, a simple coaxial nid-GaAs/n-InGaP NW (see Figure 1a), hereafter referred to as *structure A*, is transferred and analyzed via MT-STM to determine the contact-independent resistance of the n-InGaP shell along the NW axis. The four-point measurement principle with two fixed probes (1 and 4) for current injection and two probes in between (2 and 3) for the measurement of the length-dependent potential drop (one fixed, one moving) is depicted by an SEM image of a contacted NW in **Figure 2**a and as schematic inset in Figure 2b. In the latter, also the measured resistance values (black squares) are plotted against the tip distance *L* of the probes used for the potential measurement. As the potential measurement between probes 2 and 3 is highly resistive and therefore current-free, a potential drop at the probe–semiconductor interface is negligible and the measurement is contact-independent.

To estimate the doping concentration from the measurement, Equation (1) is used to model the resistance in the NW shell (q is the elemental charge).[46,47]

$$R_{\text{shell}} = \int_{\text{tip 2}}^{\text{tip 3}} \frac{l}{q \cdot \mu(N_{\text{D}}) \cdot N_{\text{D}} \cdot \overline{A}_{\text{eff}}(l, N_{\text{D}})} \, \mathrm{d}l \tag{1}$$

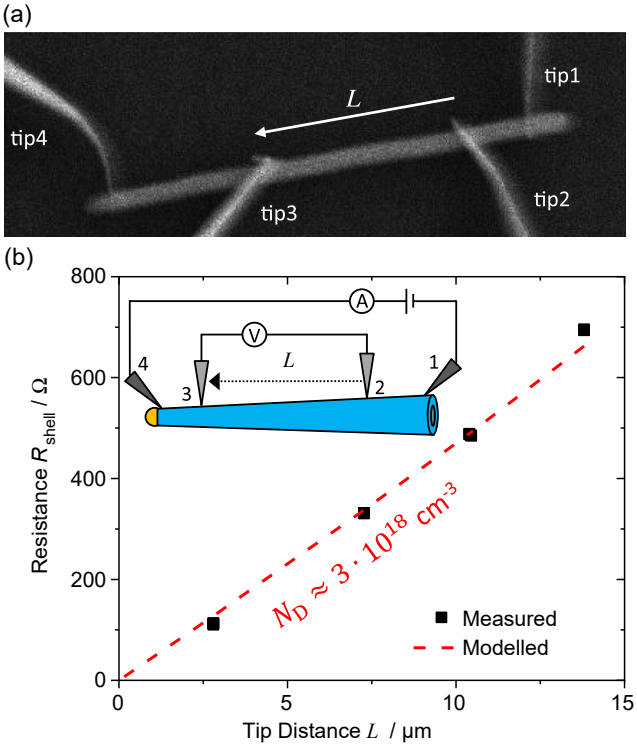

Figure 2. a) SEM image of contacted NW in a MT-STM with four tungsten tips. b) Measured and modeled length-dependent resistance of the n-InGaP shell. The schematic inset demonstrates the measurement principle, with two current-injecting probes 1 and 4 (fixed position) and probes 2 (fixed) and 3 (moving) for the distance-dependent potential measurement along the NW.

Although the shell resistance R_{shell} and the tip positions on the NW are known from the measurement, the effective cross section of the current transporting shell $\overline{A}_{eff}(l, N_D)$ and the doping-dependent electron mobility $\mu(N_D)$ have to be determined. For the radial shell growth, a homogeneous doping profile with a constant N_D along the wire is assumed.

First, the NW geometry and cross section of structure *A* is analyzed via SEM imaging to determine the core and shell thickness (see exemplary cross section Figure 1a). The total cross section of the measured NW exhibits a hexagonal shape (A_{hex}) with a varying facet width w_{shell} along the NW length of 21 µm, starting with 540 nm at the NW base and decreasing to 480 nm at the NW top. The NW cores from the sample exhibit a non-symmetric hexagonal cross section that is approximated by a triangular shape (A_{tri}). The cores are also tapered with a triangle-leg width w_{core} ranging from 370–150 nm from base to top, respectively. Both, the tapered core and shell result in a non-linear change of the shell cross section ($A_{hex} - A_{tri}$) along the NW, which is included in the modeling by averaging the shell cross section over the measured NW length. The exact probe positions on the NW and the distance between the probes are included in the resistance modeling to determine an effective current transporting shell cross section $\overline{A}_{eff}(l, N_D)$ that is kept constant for the modeling. Here, infinitesimally thin shell cross sections between the two probe tips 2 and 3 are summed up and divided by the tip distance *L*.

$$\overline{A}_{eff}(l, N_D) = \frac{\sqrt{3}}{2 \cdot L} \int_{\text{tip 2}}^{\text{tip 3}} \left(\underbrace{3 \cdot [w_{shell}(l) - d_{surf}(N_D)]^2}_{A_{hex}} - \underbrace{\frac{1}{2}[w_{core}(l) + d_{scr,n}(N_D)]^2}_{A_{tri}} \right) dl \quad (2)$$

Interface and surface depletion effects have to be considered, which might further affect $\overline{A}_{eff}$. Assuming an effective n-doping of the outer shell, the gradient in charge carriers between the shell and the nid-GaAs core (assumed p-type background doping $N_A < 1 \cdot 10^{16}$ cm^{-3}) is large and a space charge region mostly extends into the NW core (with Equation S1, Supporting Information: $d_{scr,n} < 2$ nm if $N_D = 3 \cdot 10^{18}$ cm^{-3}). Additional depletion effects at the junction by traps and/or compositional variation in the facet edges are not taken into account.

At the NW surface, depletion effects are induced by Fermi-level pinning of surface-states and result in a lack of free carriers, which reduce the current transporting area right at the NW surface. Therefore, the doping-dependent surface depletion d_{surf} is included in our modeling with a surface potential of $\varphi_s = 0.2$ V for InGaP (with Equation S2, Supporting Information: $d_{surf} < 10$ nm if $N_D = 3 \cdot 10^{18}$ cm^{-3}).[47–49]

Additional to the position-dependent current transporting cross section $\overline{A}_{eff}$, the charge carrier mobility has to be considered for the modeling. In a first approximation, the mobility μ in our NW structures is assumed to be similar to mobilities in planar n-InGaP layers. In our laboratory, Si-doped InGaP layers were grown on (100) GaAs substrates with growth parameters matching those of n-InGaP NW shells (details in experimental section 4), exhibiting a Hall mobility of 739 cm^2 V^{-1} s^{-1} at $N_D \approx 4 \cdot 10^{18}$ cm^{-3}. These values correspond well with the previously published data for MOVPE-grown n-doped InGaP layers.[50,51] A fit function through all data points is extracted to include the doping-dependent mobilities to be used in our NW resistance model (see Figure S1 and Equation S3, Supporting Information). Modeling the length-dependent shell resistance R_{shell} using Equation (1) (see dotted line in Figure 2) with respect to the NW geometry (Equation (2), S1 and S2, Supporting Information) and the doping-dependent layer mobilities (Equation S3, Supporting Information) leads to an estimated donor concentration of $N_D \approx 3 \cdot 10^{18}$ cm$^{-3} \pm 2.3 \cdot 10^{18}$ cm^{-3}. Here, the uncertainties of the dimensional determination via SEM imaging, the maximum deviation of the mobility fitting, as well as the uncertainty of the resistance measurement are taken into account to estimate the error limit. The modeled curve passes through the origin of the diagram, as expected for a resistance measurement independent of contact resistances. The established doping concentration is already useful, since the realization of Si-doped InGaP NW shell growth with N_D in the mid-10^{18} cm^{-3} range is a prerequisite for the implementation as an electron-supply shell in NW devices.

2.2. n-InGaP Shells in Core–Multishell NWs

To investigate the implementation of the n-InGaP shells in transistor devices, the following experiments are performed on

coaxial n–p–n NW-HBT structures, where the outer InGaP shell serves as an electron emitter (see Figure 1b). The n-GaAs/nid-InGaP/p-GaAs/x-InGaP/n-InGaP core–multishell NW HBTs, referred to as *structure B* in the following, are analyzed comprehensively regarding contact formation with the outer n-InGaP shell, and regarding the electrical and electro-optical behavior of the outer p-GaAs/x-InGaP/n-InGaP junction. Here, x symbolizes a varying IV/III ratio during shell growth, resulting in a step-graded doping profile of the outer InGaP shell.

2.2.1. Ohmic Contacts to n-InGaP shells

For the implementation of the n-doped InGaP shells in devices, it is necessary to deposit high-quality metallic contacts, which exhibit ohmic behavior at low bias and low specific contact resistance. To analyze the contact quality in our n–p–n devices, an annealing experiment is done using two samples with transferred NWs from the same epitaxial run (*structure B*). First, four individual Ge/Ni/Ge/Au contacts were deposited onto the outer n-InGaP shell of each NW and the contacted NWs from the two samples were investigated by four-point measurements between each neighboring contact pair. Altogether, three NWs from the first sample and six NWs from the second sample are analyzed, resulting in a total of 27 *I–V* measurements (three measurements per NW). After the first *I–V* measurements, the two samples are annealed in a rapid thermal annealing system under nitrogen atmosphere for 30 s at 320 °C (sample 1) and 30 s at 340 °C (sample 2), respectively, and then measured again. To include the influence of annealing time in our analysis, the 320 °C sample is annealed for a second time with the same parameters, and then measured for a third time.

To compare the data before and after contact annealing, the measured *I–V* curves are analyzed by linear fitting (see Figure S2, Supporting Information). To identify a measured *I–V* characteristic as ohmic, we assume a strong correlation of the linear best fit to the measured data ($R^2 > 0.99$). To account for the quality of the fitting, the corresponding correlation coefficients of the linear best fit ($R^2 = 1$ for perfect fit) are depicted as box plots in **Figure 3**a. Non-annealed Ge/Ni/Ge/Au contacts are known to form Schottky barriers at the semiconductor–metal interface with non-linear *I–V* characteristics. Therefore, for the non-annealed samples the quality of the linear fitting to the *I–V* curve is poor, with a mean correlation coefficient $R^2 \approx 0.86$ and a range of $R_2 \approx 0.6 - 0.98$. These data are taken as a reference point for the degree of improvements by annealing, causing a linearization of the *I–V* characteristics. After annealing, the overall quality of the linear fit improves for all samples, most likely due to a reduction in the Schottky barrier width caused by Ge diffusion into the semiconductor. For the sample annealed for 30 s at 320 °C, a fraction of 50 % of the measured *I–V* characteristics show ohmic behavior and most measurements exhibit R^2 values in the range of 0.97–0.99. A second annealing of the first sample with the same parameters further improves the fit quality, with 67 % of the *I–V* curves exhibiting

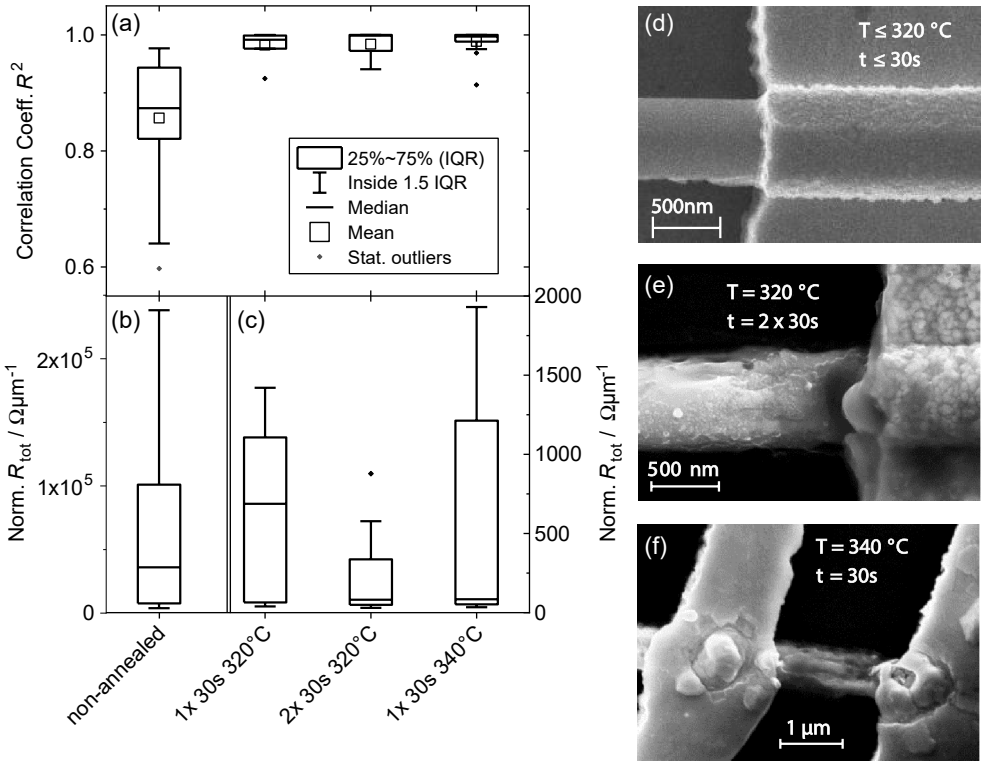

Figure 3. Analysis of the annealing set of Ge/Ni/Ge/Au contacts with n-InGaP NW shells before and after annealing at 320 and 340 °C. The diagrams show boxplots of a) the correlation coefficient R^2 of the corresponding linear fit, b) the extracted and normalized total resistances R_{tot} (shell and contacts) between two contact pairs before annealing and c) R_{tot} after annealing. d–f) show SEM images of annealed contacts with n-InGaP after different annealing temperatures *T* and times *t*.

ohmic behavior. To account for the influence of the annealing temperature, a second sample is annealed for 30 s at 340 °C. Here, 67 % of the *I*–*V* plots are ohmic and nearly 85 % of the fits show $R^2 > 0.98$.

The slope of the linear fit functions before and after annealing gives additional information about the total resistance, which consists of the contact resistances of the contact pair and the path resistance of the shell material in between. The extracted R_{tot} (normalized to 1 µm NW length) for each measurement are depicted as boxplots in Figure 3b and c. Before annealing, the estimated resistance values by linear fitting are spread over three orders of magnitude between $3750\,\Omega\,\mu m^{-1}$ and $2.5 \times 10^6\,\Omega\,\mu m^{-1}$, with a median of $36\,k\Omega\,\mu m^{-1}$ (Figure 3b). Annealing shifts the extracted values for all samples to lower resistances (Figure 3c). In conjunction with the higher fit quality, this indicates improved contacts, particularly for the samples with higher annealing temperature or longer annealing times, where the median drops down to $\approx 90\,\Omega\,\mu m^{-1}$. Longer annealing times or higher annealing temperatures seem beneficial for the formation of ohmic contacts to n-InGaP. However, while beneficial Ge diffusion into the semiconductor increases with rising annealing temperature or time, simultaneously part of the Ga outdiffuses from the NW into the metal contact. Due to the NW geometry, the semiconductor thickness below the deposited contacts is small, and increased Ga diffusion can lead to severe damage of the NW, including damage to the underlying p–n junction.[45] In Figure 3d–f three SEM micrographs of annealed contacts to n-InGaP NW shells are depicted. Although the NW surface of samples annealed at ≤320 °C for 30 s (Figure 3d) did not exhibit remarkable change, a second annealing at the same temperature (Figure 3e) or higher annealing temperatures (Figure 3f) resulted in a degradation of the NW regions near the contacts: the semiconducting material between the contacts has deteriorated, while simultaneously the contacts are broadened in the region above the NW. Although annealing at 320 °C for 60 s provides the best electrical results, the effects on the NW morphology cannot be neglected and lower annealing temperatures or times are advised. Low temperatures are especially important, if thin NW shells are contacted, due to the diffusion coefficient's temperature relation.[52]

2.2.2. Doping Dependent p–n Junction Characteristics

The established n-doping in InGaP NW shells and ohmic contacts to these, facilitate the use as wide band gap electron-supplying material in a p–n junction. NWs with *structure B* are used to analyze the outer p-GaAs/x-InGaP/n-InGaP junction (p–n junction + cap shell, see Figure 1b). A step-graded doping profile is introduced by variation of the ditertiarybutylsilane (DitBuSi) flow during growth of the x-InGaP shell to analyze the influence of doping on the current density *J* when bias is applied. The maximum DitBuSi flow in these experiments (hereafter referred to as 100 %) corresponds to a IV/III-ratio of $9.4 \cdot 10^{-3}$, resulting in the estimated doping concentration $N_D \approx 3 \cdot 10^{18}\,cm^{-3}$ (section 2.1). Four samples were grown and processed with 100 % (24 NWs), 50 % (23 NWs), 10 % (27 NWs), and 0 % (25 NWs) DitBuSi flow during x-InGaP shell growth, respectively. Semi-logarithmically scaled *J*–*V* characteristics of exemplary NWs of the four different samples are depicted in **Figure 4**a. All other material parameters (thickness and doping) remain constant for all the samples. For the analysis of the outer p–n junction, the x-InGaP/n-InGaP shells on the upper half of the wires are selectively wet etched to access the p-material in the intermediate shell. The wires are then transferred to insulating substrates and individual contacts are deposited onto the p-GaAs and n-InGaP shells. An exemplary SEM image of a contacted NW p–n junction is shown in Figure 4b. After annealing, the contacts are assumed to be ohmic and *J*–*V* characteristics are measured, with positive bias applied to the p-contact and the n-contact grounded.

For the sample with the 100 % DitBuSi flow during x-InGaP shell growth, the current density under reverse bias is higher than under forward bias, resulting in a rectification ratio <1 (dotted curve in Figure 4a). The same effect was observed before in planar GaAs diodes with donor concentrations in the mid- and upper-$10^{18}\,cm^{-3}$ range and can be associated with increased tunneling currents under reverse bias due to a larger electric field inside the junction.[53] With decreasing doping of the intermediate x-InGaP shell, the reverse current density decreases significantly. Comparing the highly doped sample (100 %) with the nid-sample (0 %), the drop in reverse current density amounts to almost three orders of magnitude at $V = -1$ V. The current

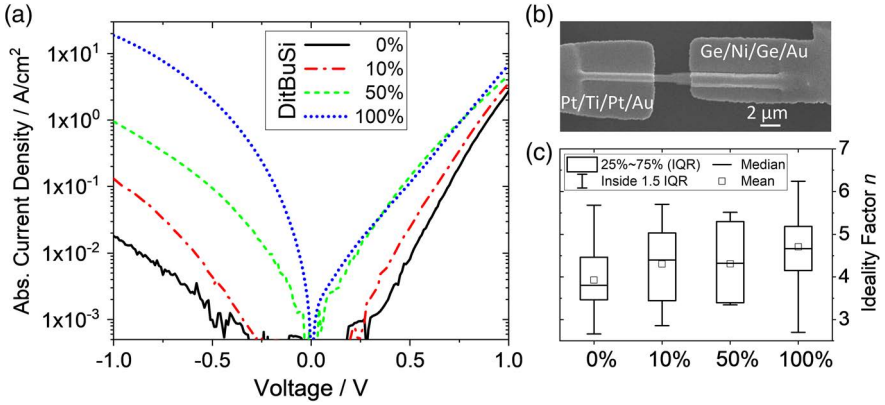

Figure 4. Analysis of coaxial p-GaAs/x-InGaP/n-InGaP heterojunctions with varying DitBuSi flow during x-InGaP growth. a) Semi-logarithmically scaled absolute current density *J* versus applied voltage *V*. b) SEM image of a contacted NW. c) Boxplot of extracted ideality factors.

density under forward bias also decreases slightly with lower dopant flow during growth. The change in current density under forward and reverse bias affects the rectifying behavior of the junction resulting in a rectification ratio >100 for the nid-sample at absolute bias of $|V| = 1$ V. But, even for this sample the current blocking under reverse bias is poor: a reverse current density of $J \approx 0.02$ A cm^{-2} at bias $V = -1$ V was measured and the reverse saturation current density was estimated from the forward J–V characteristics as $J_0 = 1.5 \cdot 10^{-5}$ A cm^{-2}. In planar GaAs/InGaP base emitter junctions with an emitter doping concentration $N_D \approx 3 \cdot 10^{17}$ cm^{-3}, J_0 is much smaller and is in the range of 10^{-18} A cm^{-2}.[54] As the doping concentrations in the base and emitter of the analyzed NW are smaller, compared with the planar device, and the saturation current densities exceed those in the planar system by many orders of magnitude, additional transport mechanisms are considered. From the data, there is clear evidence for doping-dependent current transport mechanisms occurring in the outer p–n junction under forward and reverse bias, which are attributed to tunneling processes previously observed in planar GaAs diodes.[53]

The analysis of the ideality factors can provide further insight into possible tunneling mechanisms in the analyzed structures, as ideality factors >2 can be associated with tunneling currents through defect levels.[55] In planar InGaN/AlGaN LEDs, ideality factors of 6.8 are reported and linked to the tunneling processes.[56] In general, core–shell NW can suffer from high defect densities or inhomogeneous composition, especially in the edges of the hexagonal facets of ternary material (see cross section in Figure 1b), which can promote tunneling processes.[55,57,58] The extracted ideality factors n plotted in Figure 4c show for all samples values larger than 2, which is beyond the model of Shockley–Read–Hall recombination. Comparison between the differently doped samples shows a tendency of smaller n with lower dopant flow. Here, the mean n drops from 4.7 (100 %) to 3.9 (0 %). It is suggested that the current through the diode is a superposition of a thermionic and a tunneling contribution and this decrease in n is attributed to a reduction in tunneling processes through the junction. However, even for the nid-sample the values are >2 and tunneling processes are likely to occur. These tunneling processes can severely limit the current gain in possible NW-HBTs and need further investigation.

2.2.3. Electroluminescence of p-GaAs/n-InGaP NW Junctions

To gain further insight into the recombination behavior of the previously discussed junctions with doping-dependent J–V characteristics, electroluminescence (EL) measurements at room and cryogenic temperatures are conducted on a NW with highly doped x-InGaP (100 %). Here, the reverse currents and ideality factors are the highest, and tunneling is assumed as the dominant current transport mechanism. For the measurements, the NW sample is glued and wire-bonded to a ceramic chip carrier. In **Figure 5**a, temperature-dependent EL spectra are depicted. All spectra are measured at constant external forward bias of $V = 2.4$ V.

In the spectrum measured at 300 K, a pronounced GaAs band gap luminescence ($E_g = 1.42$ eV) is apparent due to the large valence band discontinuity at the heterojunction, which prevents holes flowing from p-GaAs into the n-doped shell such that recombination only occurs in the p-doped GaAs and accordingly no luminescence signal is measured in the energy range of the band gap energy of InGaP around 1.9 eV.

The low-temperature spectra measured in the temperature range 79 K $\leq T \leq$ 210 K give further insight into the low-energy portion of the EL spectrum. With lower temperatures, the intensity of the band gap luminescence decreases significantly and shifts to higher energies, as described by the Varshni relation (see arrow in Figure 5a).[59] Below $T = 210$ K, no band gap luminescence is detected. Simultaneously, underlying peaks at the low-energy side increase in intensity and shift to lower energies. Pronounced sub-bandgap EL has been observed in heavily doped GaAs p–n-homojunctions in layers and axial NWs and was reported in compositionally graded planar GaAs/AlGaAs heterojunctions previously.[60–66] This luminescence is linked to radiative tunneling mechanisms, such as band-filling or photon-assisted tunneling. The former is based on the recombination from filled band-tail states on the p-side with electrons from the n-side, whereas the latter is strongly dependent on the displacement of the quasi Fermi levels with respect to each other.[61,64,67] Both mechanisms can occur in p–n junctions biased forward below the diffusion voltage ($V < V_{diff}$), where tunneling into the bandgap is possible. Due to the high resistive

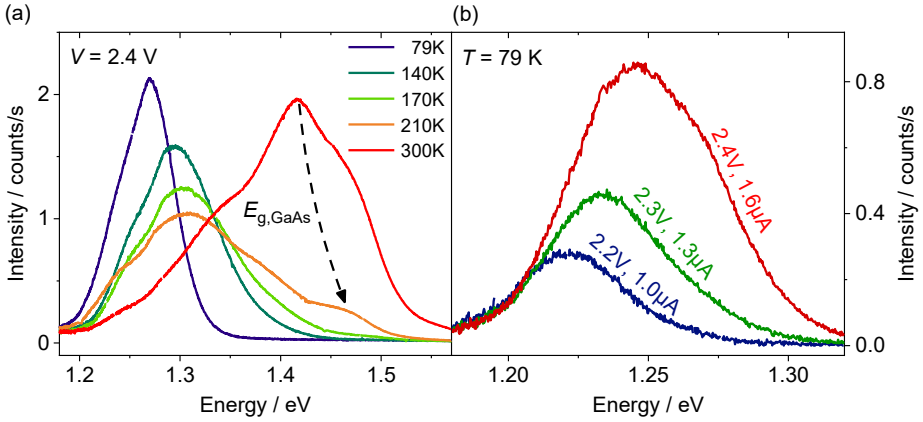

Figure 5. EL spectra of a NW with 100 % DitBuSi flow during x-InGaP growth. a) Temperature-dependent EL intensity versus energy at bias $V = 2.4$ V. b) Voltage-dependent EL intensity versus energy at $T = 79$ K.

nature of NWs, we assume that the internal diffusion potential of the p–n junction is not reached at the applied bias ($V = 2.4$ V), although currents in the lower μA range are flowing. The band-edge emission itself is based on an increased occupation of the states above the Fermi level with rising temperature, therefore thermal injection is possible even below V_{diff}.[64] Similarly, the broadening of the sub-band gap emission peak with higher temperatures is attributed to an increased energy distribution of free carriers.

To further substantiate the assumed tunneling processes, low-temperature EL measurements with varying bias are conducted at a fixed temperature $T = 79$ K. The resulting spectra are displayed in Figure 5b. As previously observed for radiative tunneling processes in abrupt p–n-homojunctions, the maximum peak intensities shift to higher energies with increasing excitation current, and the low-energy side of the spectrum is saturated while the peak itself broadens with rising current.[64,66,68] The observed sub-band gap EL at low temperatures and its shift with applied bias are strong indications for dominant radiative tunneling currents through the p–n-heterojunction under forward bias. However, the detected EL at room temperature is a verification of the successful formation of the p-GaAs/n-InGaP heterojunction with a hole-blocking character.

3. Conclusion

The electrical and electro-optical properties of n-doped InGaP NW shells in radial GaAs/InGaP NWs are investigated. By measuring and modeling the length-dependent shell resistance in a nid-GaAs/n-InGaP core–shell structure via MT-STM technique, we estimated the Si donor concentration in the InGaP shell to $N_D \approx 3 \cdot 10^{18}$ cm^{-3}. Subsequently, these InGaP shells were implemented as the outermost shell in a GaAs/InGaP NW-HBT structure. The possible formation of ohmic Ge/Ni/Ge/Au contacts with n-doped InGaP shells at annealing temperatures ≥ 320 °C is demonstrated. However, depending on the annealing temperature and time, excessive morphological alterations of the NW surface are possible, demonstrating a trade-off between the desired high contact quality and structural intactness of the NW. Application of the Ge/Ni/Ge/Au contacts to p-GaAs/n-InGaP NW junctions was demonstrated by the electrical and electro-optical characterization of the said junctions via DC and EL measurements. Radiative tunneling currents through the junctions are observed under forward bias and relate to high defect densities and doping concentrations. These leakage currents limit the applicability in devices, especially in those sensitive to leakage currents such as HBTs, as tunneling currents in the base emitter diode are expected to contribute to the base current and thus limiting the possible current gain of the device. A deeper understanding of the tunneling currents in these coaxial diodes is a prerequisite to realize and improve current amplifying NW transistor structures.

4. Experimental Section

NW Growth: Coaxial GaAs/InGaP NWs were fabricated in an AIX200 RF MOVPE reactor via vapor–liquid–solid and vapor–solid growth mode. As growth catalysts, Au particles with a size of 100 nm were randomly deposited on a Si-doped (111)B GaAs growth substrate via spin-coating of a colloidal solution. For the GaAs core growth of both, *structure A* and *structure B*, the precursors tertiarybutylarsine (TBAs) and trimethylgallium (TMGa) were used (V/III = 2.5) at a growth temperature of $T = 450$ °C resulting in a growth rate of approximately 3 nm s^{-1}. As the dopant for the n-GaAs core of structure B, tetraethyltin (TESn) was supplied 5 min before and during the growth (IV/III = 0.08) to achieve homogenous doping of $N_{D,GaAs} = 1 \cdot 10^{18}$ cm^{-3}.[45,69]

For all NW shells, growth occurred at growth temperatures $T = 650$ °C. The nid- and n-doped InGaP shells were grown using tertiarybutylphosphine (TBP) and trimethylindium (TMIn) along with TMGa. The V/III-ratios were 26.4 (nid) and 30.1 (n), respectively. The n-doping was achieved by adding DitBuSi with the IV/III-ratios $9.4 \cdot 10^{-3}$ (defined as 100 % DitBuSi flow), $4.7 \cdot 10^{-3}$ (50 % DitBuSi flow), and $9.4 \cdot 10^{-4}$ (10 % DitBuSi flow). TMGa and TBAs were used as precursors for the p-doped GaAs shell in *structure B* (V/III = 4.9) with tetrabrommethane (CBr_4) as dopant (IV/III = 0.3) which resulted in an acceptor concentration $N_{A,GaAs} = 2.5 \cdot 10^{18}$ cm^{-3}.

NW Processing: The samples with *structure B* were height-controlled, embedded in photoresist, and selectively wet etched with a process scheme described earlier.[18] For the characterization of the different structures, all NWs were transferred to insulating substrates and embedded in an insulating polyimide (Fujifilm Durimide 7500) to overcome the topology difference. Subsequently, individual contacts onto p- and n-regions were defined via electron-beam lithography.[18] The native oxide at the NW surface was removed with HCl:H_2O (1:4), followed by evaporation of Pt/Ti/Pt/Au (50/100/100/4000 nm) and Ge/Ni/Ge/Au (2/20/50/400 nm) as multilayer contacts onto the p- and n-doped NW regions, respectively.

MT-STM Technique: By using four independently movable tungsten tips, which were controlled via piezoelectric nanopositioners, the NWs were electrically characterized non-destructively in a UHV chamber. The tips were sputtered before measurement to remove their oxide coverage. The electrical investigations were performed by using transimpedance amplifier and custom-built electronics for each tip. This setup enabled the switching between low-impedance current measurements and high-impedance voltage probing.[70] An integrated SEM enabled the visualization of the tips and NWs.

Supporting Information

Supporting Information is available from the Wiley Online Library or from the author.

Acknowledgements

This work was supported by the German Research Foundation (DFG) under research grant 265982007 and project no. HA3096 (grant 403523188). The authors thank R. Geitmann for his commitment to the MOVPE nanowire growth. The authors also thank R. Röder from Friedrich Schiller University Jena for the STEM imaging.

Conflict of Interest

The authors declare no conflict of interest.

Keywords

core–shell nanowires, GaAs, InGaP, p–n junctions

Received: June 25, 2019
Revised: July 23, 2019
Published online: September 4, 2019

[1] M. S. Gudiksen, L. J. Lauhon, J. Wang, D. C. Smith, C. M. Lieber, *Nature* **2002**, *415*, 617.
[2] A. Kikuchi, M. Kawai, M. Tada, K. Kishino, *Jpn. J. Appl. Phys.* **2004**, *43*, 1524.
[3] I. Regolin, C. Gutsche, A. Lysov, K. Blekker, Z.-A. Li, M. Spasova, W. Prost, F.-J. Tegude, *J. Cryst. Growth* **2011**, *315*, 143.
[4] J. V. Holm, H. I. Jørgensen, P. Krogstrup, J. Nygård, H. Liu, M. Aagesen, *Nat. Commun.* **2013**, *4*, 1.
[5] C. P. T. Svensson, T. Mårtensson, J. Trägårdh, C. Larsson, M. Rask, D. Hessman, L. Samuelson, J. Ohlsson, C. Patrik, T. Svensson, T. Mårtensson, J. Trägårdh, C. Larsson, M. Rask, D. Hessman, L. Samuelson, J. Ohlsson, *Nanotechnology* **2008**, *19*, 305201.
[6] M. D. Brubaker, K. L. Genter, A. Roshko, P. T. Blanchard, B. T. Spann, T. E. Harvey, K. A. Bertness, *Nanotechnology* **2019**, *30*, 234001.
[7] M. Mandl, X. Wang, T. Schimpke, C. Kölper, M. Binder, J. Ledig, A. Waag, X. Kong, A. Trampert, F. Bertram, J. Christen, F. Barbagini, E. Calleja, M. Strassburg, *Phys. Status Solidi RRL* **2013**, *7*, 800.
[8] I. Åberg, G. Vescovi, D. Asoli, U. Naseem, J. P. Gilboy, C. Sundvall, A. Dahlgren, K. E. Svensson, N. Anttu, M. T. Björk, L. Samuelson, *IEEE J. Photovolt.* **2016**, *6*, 185.
[9] F. Glas, in *Semiconductor Nanowires I: Growth and Theory* (Eds: A. Fontcuberta i Morral, S. A. Dayeh, C. Jagadish), Semiconductors and Semimetals Vol. 93, Academic Press, Inc., London, UK **2015**, Ch. 2.
[10] L. C. Chuang, M. Moewe, C. Chase, N. P. Kobayashi, C. Chang-Hasnain, S. Crankshaw, *Appl. Phys. Lett.* **2007**, *90*, 2005.
[11] N. Huang, M. L. Povinelli, *IEEE J. Photovolt.* **2014**, *4*, 1511.
[12] B. Hua, J. Motohisa, Y. Kobayashi, S. Hara, T. Fukui, *Nano Lett.* **2009**, *9*, 112.
[13] C. Ghezzi, R. Magnanini, A. Parisini, L. Tarricone, *Phys. Rev. B* **2008**, *77*, 125317.
[14] A. C. Farrell, P. Senanayake, X. Meng, N. Y. Hsieh, D. L. Huffaker, *Nano Lett.* **2017**, *17*, 2420.
[15] D. Saxena, N. Jiang, X. Yuan, S. Mokkapati, Y. Guo, H. H. Tan, C. Jagadish, *Nano Lett.* **2016**, *16*, 5080.
[16] Y. Chen, M.-E. Pistol, N. Anttu, *Sci. Rep.* **2016**, *6*, 32349.
[17] M. Steidl, C. Koppka, L. Winterfeld, K. Peh, B. Galiana, O. Supplie, P. Kleinschmidt, E. Runge, T. Hannappel, *ACS Nano* **2017**, *11*, 8679.
[18] L. Liborius, F. Heyer, K. Arzi, C. Speich, W. Prost, F. Tegude, N. Weimann, A. Poloczek, *Phys. Status Solidi A* **2019**, *216*, 1800562.
[19] C. Blömers, T. Grap, M. I. Lepsa, J. Moers, S. Trellenkamp, D. Grützmacher, H. Lüth, T. Schäpers, *Appl. Phys. Lett.* **2012**, *101*, 152106.
[20] K. Storm, F. Halvardsson, M. Heurlin, D. Lindgren, A. Gustafsson, P. M. Wu, B. Monemar, L. Samuelson, *Nat. Nanotechnol.* **2012**, *7*, 718.
[21] O. Hultin, G. Otnes, M. T. Borgström, M. Björk, L. Samuelson, K. Storm, *Nano Lett.* **2016**, *16*, 205.
[22] M. Heurlin, O. Hultin, K. Storm, D. Lindgren, M. T. Borgström, L. Samuelson, *Nano Lett.* **2014**, *14*, 749.
[23] D. Lindgren, O. Hultin, M. Heurlin, K. Storm, M. T. Borgström, L. Samuelson, A. Gustafsson, *Nanotechnology* **2015**, *26*, 045705.
[24] F. Haas, P. Zellekens, M. Lepsa, T. Rieger, D. Grützmacher, H. Lüth, T. Schäpers, *Nano Lett.* **2017**, *17*, 128.
[25] S. E. Mohney, Y. Wang, M. A. Cabassi, K. K. Lew, S. Dey, J. M. Redwing, T. S. Mayer, *Solid State Electron.* **2005**, *49*, 227.
[26] G. K. Reeves, H. B. Harrison, *IEEE Electron Device Lett.* **1982**, *EDL-3*, 111.
[27] A. Nägelein, L. Liborius, M. Steidl, C. Blumberg, P. Kleinschmidt, A. Poloczek, T. Hannappel, *J. Phys.: Condens. Matter* **2017**, *29*, 394007.
[28] Y. Cui, X. Duan, J. Hu, C. M. Lieber, *J. Phys. Chem. B* **2000**, *104*, 5213.
[29] J. Wallentin, M. T. Borgström, *J. Mater. Res.* **2011**, *26*, 2142.
[30] R. Tu, L. Zhang, Y. Nishi, H. Dai, *Nano Lett.* **2007**, *7*, 1561.
[31] J. W. W. van Tilburg, R. E. Algra, W. G. G. Immink, M. Verheijen, E. P. A. M. Bakkers, L. P. Kouwenhoven, *Semicond. Sci. Technol.* **2010**, *25*, 024011.
[32] H. Park, R. Beresford, S. Hong, J. Xu, *J. Appl. Phys.* **2010**, *108*, 094308.
[33] E. H. Rhoderick, *Phys. Technol.* **1974**, *5*, 223.
[34] C. Liu, L. Dai, L. P. You, W. J. Xu, G. G. Qin, *Nanotechnology* **2008**, *19*, 465203.
[35] J. Wallentin, K. Mergenthaler, M. Ek, L. R. Wallenberg, L. Samuelson, K. Deppert, M.-E. Pistol, M. T. Borgström, *Nano Lett.* **2011**, *11*, 2286.
[36] M. Hilse, M. Ramsteiner, S. Breuer, L. Geelhaar, H. Riechert, *Appl. Phys. Lett.* **2010**, *96*, 193104.
[37] B. Ketterer, E. Uccelli, A. Fontcuberta i Morral, *Nanoscale* **2012**, *4*, 1789.
[38] J. J. Boland, S. Conesa-Boj, P. Parkinson, G. Tütüncüoglu, F. Matteini, D. Rüffer, A. Casadei, F. Amaduzzi, F. Jabeen, C. L. Davies, H. J. Joyce, L. M. Herz, A. Fontcuberta i Morral, M. B. Johnston, *Nano Lett.* **2015**, *15*, 1336.
[39] P. De Wolf, R. Stephenson, T. Trenkler, T. Clarysse, T. Hantschel, W. Vandervorst, *J. Vac. Sci. Technol. B Microelectron. Nanom. Struct.* **2000**, *18*, 361.
[40] D. Mikulik, M. Ricci, G. Tutuncuoglu, F. Matteini, J. Vukajlovic, N. Vulic, E. Alarcon-Llado, A. Fontcuberta i Morral, *Nano Energy* **2017**, *41*, 566.
[41] S. Korte, M. Steidl, W. Prost, V. Cherepanov, B. Voigtländer, W. Zhao, P. Kleinschmidt, T. Hannappel, *Appl. Phys. Lett.* **2013**, *103*, 143104.
[42] V. Cherepanov, E. Zubkov, H. Junker, S. Korte, M. Blab, P. Coenen, B. Voigtländer, *Rev. Sci. Instrum.* **2012**, *83*, 033707.
[43] F. Ren, J. M. Kuo, S. J. Pearton, T. R. Fullowan, J. R. Lothian, *J. Electron. Mater.* **1992**, *21*, 243.
[44] C.-Y. Chai, J.-W. Wu, J.-D. Guo, J.-A. Huang, Y.-L. Lai, S.-H. Chan, C.-Y. Chang, Y.-J. Chan, H.-C. Cheng, *Jpn. J. Appl. Phys.* **1996**, *35*, 2073.
[45] C. Gutsche, A. Lysov, I. Regolin, A. Brodt, L. Liborius, J. Frohleiks, W. Prost, F.-J. Tegude, *J. Appl. Phys.* **2011**, *110*, 014305.
[46] C. Gutsche, I. Regolin, K. Blekker, A. Lysov, W. Prost, F.-J. Tegude, *J. Appl. Phys.* **2009**, *105*, 024305.
[47] A. C. E. Chia, R. R. Lapierre, *J. Appl. Phys.* **2012**, *112*, 063705.
[48] Y. Tkachenko, Y. Zhao, C. Wei, D. Bartle, *Microw. J.* **2001**, *44*, 122.
[49] B. S. Simpkins, M. A. Mastro, C. R. Eddy, P. E. Pehrsson, *J. Appl. Phys.* **2008**, *103*, 104313.
[50] F. Scheffer, F. Buchali, A. Lindner, Q. Liu, A. Wiersch, W. Prost, *J. Cryst. Growth* **1992**, *124*, 475.
[51] Y. Ohba, M. Ishikawa, H. Sugawara, M. Yamamoto, T. Nakanisi, *J. Cryst. Growth* **1986**, *77*, 374.
[52] W. Jost, *Diffusion in solids, liquids, gases*, Academic Press, Inc., New York **1960**.
[53] D. J. Dumin, G. L. Pearson, *J. Appl. Phys.* **1965**, *36*, 3418.
[54] R. Loga, A. Vilches, *Semicond. Sci. Technol.* **2004**, *19*, 408.
[55] A. Schenk, U. Krumbein, *J. Appl. Phys.* **1995**, *78*, 3185.
[56] H. C. Casey, J. Muth, S. Krishnankutty, J. M. Zavada, *Appl. Phys. Lett.* **1996**, *68*, 2867.
[57] D. Rudolph, S. Funk, M. Döblinger, S. Morkötter, S. Hertenberger, L. Schweickert, J. Becker, S. Matich, M. Bichler, D. Spirkoska, I. Zardo, J. J. Finley, G. Abstreiter, G. Koblmüller, *Nano Lett.* **2013**, *13*, 1522.
[58] L. Gagliano, A. Belabbes, M. Albani, S. Assali, M. A. Verheijen, L. Miglio, F. Bechstedt, J. E. M. Haverkort, E. P. A. M. Bakkers, *Nano Lett.* **2016**, *16*, 7930.
[59] Y. P. Varshni, *Physica* **1967**, *34*, 149.
[60] T. J. De Lyon, H. C. Casey, P. M. Enquist, J. A. Hutchby, A. J. SpringThorpe, *J. Appl. Phys.* **1989**, *65*, 3282.
[61] J. I. Pankove, *Phys. Rev. Lett.* **1962**, *9*, 283.

[62] R. J. Archer, A. C. C. Leite, A. Yariv, S. P. S. Porto, J. M. Whelan, *Phys. Rev. Lett.* **1963**, *10*, 483.
[63] T. N. Morgan, *Phys. Rev.* **1966**, *148*, 890.
[64] H. C. Casey, D. J. Silversmith, *J. Appl. Phys.* **1969**, *40*, 241.
[65] A. Lysov, M. Offer, C. Gutsche, I. Regolin, S. Topaloglu, M. Geller, W. Prost, F.-J. Tegude, *Nanotechnology* **2011**, *22*, 085702.
[66] J. Motohisa, H. Kameda, M. Sasaki, K. Tomioka, *Nanotechnology* **2019**, *30*, 134002.
[67] D. F. Nelson, M. Gershenzon, A. Ashkin, L. A. D'Asaro, J. C. Sarace, *Appl. Phys. Lett.* **1963**, *2*, 182.
[68] A. Lysov, C. Gutsche, M. Offer, I. Regolin, W. Prost, F.-J. Tegude, *Device Res. Conf. - Conf. Dig. DRC* **2011**, *4*, 53.
[69] C. Gutsche, A. Lysov, D. Braam, I. Regolin, G. Keller, Z. A. Li, M. Geller, M. Spasova, W. Prost, F.-J. Tegude, *Adv. Funct. Mater.* **2012**, *22*, 929.
[70] R. Hobara, N. Nagamura, S. Hasegawa, I. Matsuda, Y. Yamamoto, Y. Miyatake, T. Nagamura, *Rev. Sci. Instrum.* **2007**, *78*, 053705.